Oceanologia, 67 (3)/2025, 67307
Polish Academy of Sciences
Institute of Oceanology

https://doi.org/10.5697/MUOD6431

Oceanic response to super typhoon based on simulation by FVCOM and SWAN

Lu Liu[1], Yuyi Hu[1] Weizeng Shao[1,*], Ru Yao[1], Guanyin Lin[2], Weili Wang[3]

Abstract
The South China Sea is a region frequently impacted by intense tropical cyclones (TCs). Recent super typhoons such as Yagi (2024), Haikui (2023), Saola (2023), Doksuri (2023), and Koinu (2023) have caused catastrophic damage. This study primarily investigates the oceanic response to westward-moving super typhoons. The cyclonic wind field is reconstructed based on reanalysis from the European Centre for Medium-Range Weather Forecasts (ECMWF), and the TC wind speed derived from measurements of five moored buoys shows a 4.01 m/s root mean squared error (RMSE), a 0.90 Pearson's correlation (Cor), and a 0.48 scatter index (SI). A triangular-grid-based numerical circulation mode, namely the Finite-Volume Community Ocean Model (FVCOM), is employed to simulate sea surface currents and sea levels. The reconstructed TC winds act as the forcing field, and the FVCOM-simulated sea surface currents and sea levels are then incorporated into wave simulations conducted with the Simulating WAves Nearshore (SWAN) model. It is found that the hindcasting significant wave heights (SWHs) are most consistent with measurements from moored buoys when current and sea level are included, and this phenomenon is particularly significant around the Taiwan Strait. Two parameterizations of the drag coefficient C_d, i.e., the C_d by Wu (1982) and the C_d by Hu et al. (2024), are used in SWAN. The improved C_d shows a clear advantage when SWH $>$ 3 m, resulting in a reduction of over-estimation and an increase in SWH accuracy by 0.6 m. Wind and SWH exhibit opposing asymmetry trends due to swell influence. Along super typhoon tracks, sea surface temperature (SST) cooling reaches a maximum of 4°C; however, the Kuroshio Current and Zhejiang-Fujian Coastal Current mitigate this cooling, reducing it by approximately 1°C. These findings offer significant implications for understanding super typhoon responses to ocean dynamics and provide critical insights for enhancing disaster resilience strategies during extreme weather events.

Keywords
Wave; FVCOM; SWAN; Super typhoon

[1] *College of Oceanography and Ecological Science, Shanghai Ocean University, Shanghai, China*
[2] *South China Sea Survey Center, Ministry of Natural Resources, Guangzhou, China*
[3] *Hainan Observation and Research Station of Ecological Environment and Fishery Resource in Yazhou Bay, Hainan Institute of Zhejiang University, Sanya, China*
***Correspondence**: wzshao@shou.edu.cn (W. Shao)

Received: 2 December 2024; **revised:** 19 May 2025; **accepted**: 18 August 2025

1. Introduction

It is widely recognized that tropical cyclones (TCs) bring strong winds, extreme sea states, and heavy precipitation. Super Typhoon Yagi (2024), the second-strongest typhoon on record in China, made landfall near Hainan Island with catastrophic impacts.

In the context of climate change, the intensity of TCs has increased by approximately 5% from 1998 to 2017, and the tracks of TCs show a tendency to shift northward since 2004 (Hu et al., 2021; Huang et al., 2024). Therefore, TCs pose a serious threat to coastal areas. In the literature, continuous data from moored buoys, such as those from the National Data Buoy Center (NDBC) (Steele et al., 1985), are considered reliable for oceanographic studies. However, near real-time measurements during TCs are scarce, primarily because of the considerable distance between TC centers and nearshore buoys. Additionally, in-situ observations lack the spatial coverage needed for comprehensive wave distribution analysis (Yao et al., 2023).

Since the 1990s, remotely sensed products have significantly advanced the progress of oceanography theory, as oceanic dynamics over the global oceans can be routinely monitored by space-borne satellites operating at microwave frequencies (Boutin and Etcheto, 1990). For instance, sea surface winds can be detected by scatterom-

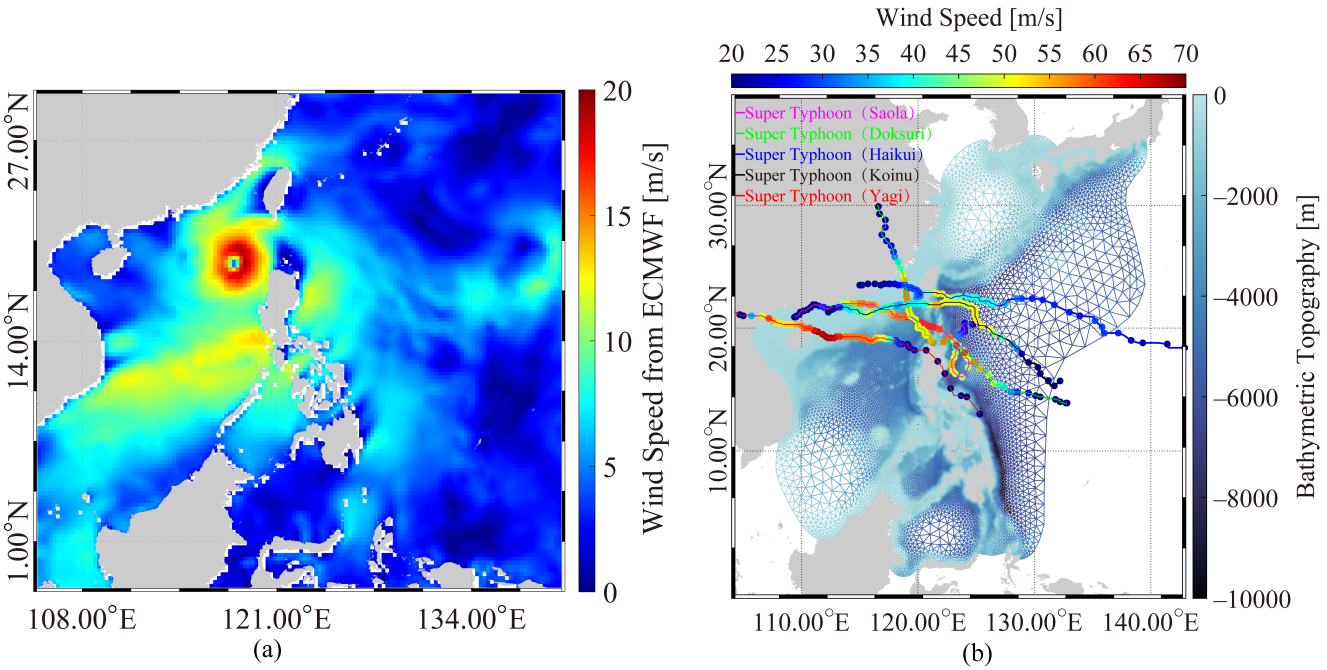

Figure 1. European Centre for Medium-Range Weather Forecasts (ECMWF) wind field at 00:00 UTC on 4 September 2024, with the best track of Super Typhoon Yagi (2024) (Shanghai Meteorological Bureau) shown as a black line (a). Computational domain with triangular mesh overlaid on General Bathymetric Chart of the Oceans (GEBCO) bathymetry, showing tracks of five tropical cyclones (TCs): Doksuri (2023), Saola (2023), Koinu (2023), and Haikui (2023) (b).

eters (Vogelzang and Stoffelen, 2017; Shao et al., 2021) and microwave radiometers (Wentz, 1992). These wind products have a swath coverage of up to 1000 km with a spatial resolution of about 25 km, making them applicable during a TC (Meissner et al., 2017; Chen et al., 2024). Sea surface waves are measured using satellite altimeters (Zhang et al., 2003) and the Surface Waves Investigation and Monitoring (SWIM) instrument (Hauser et al., 2017; Hao et al., 2023). Recent research (Shi et al., 2023) demonstrates that remotely sensed winds derived from combined scatterometer and microwave radiometer data can effectively serve as input for wave hindcasting in numerical models.

With the rapid growth of computer technology and oceanography theory, numerical models hold great potential for hindcasting and predicting ocean dynamics. In general, numerical models are specifically developed for simulating circulation and waves. Numerical circulation models using rectangular grids mainly include the Parallel Ocean Model (POM) (Nittis et al., 2006) with a parallel version called the Stony Brook Parallel Ocean Model (sbPOM) (Wei et al., 2024), the Nucleus for European Modelling of the Ocean (NEMO) (Stepanov and Haines, 2014), the Hybrid Coordinate Ocean Model (HYCOM) (Yao and Johns, 2010), and the Hamburg Shelf Ocean Model (HAMSOM) (Wei et al., 2004). Additionally, the Finite-Volume Community Ocean Model (FVCOM) (Chen et al., 2003) utilizes a triangular grid, which is well-suited for representing complex coastal features. Currently, WAVEWATCH III (WW3) (Tolman, 1991) and Simulating WAves Nearshore (SWAN) (Holthuijsen, 2001) are the most widely used wave models. WW3 typically employs a rectangular grid, offering high

Table 1. Detailed information on five super typhoons.

Typhoon	Time range	Max wind speed (m/s)	Minimum center pressure (Pa)
Doksuri	2023-07-21 00:00 UTC – 2023-07-29 00:00 UTC	62	915
Saola	2023-08-24 06:00 UTC – 2023-09-03 06:00 UTC	62	915
Haikui	2023-08-28 00:00 UTC – 2023-09-06 06:00 UTC	52	935
Koinu	2023-09-29 18:00 UTC – 2023-10-09 09:00 UTC	55	930
Yagi	2024-09-01 12:00 UTC – 2024-09-08 06:00 UTC	68	905

Table 2. Settings for the Finite-Volume Community Ocean Model (FVCOM).

Forcing filed	ECMWF-based reconstructed wind with a spatial resolution of 0.25° and a time interval of 1 hour.
Open boundary	Water-tide data from TPXO.7; Water temperature, water salinity, water elevation, and water current from the CMEMS with a spatial resolution of 0.08° and a time interval of 6 hours.
Spatial resolution	In the horizontal direction, the unstructured grid consists of 56 632 computational nodes and 107 082 triangular grids with the finest grid resolution of 51.615 m in the South China Sea. In the vertical direction, a total of 45 sigma layers are used.
Initial field	Water temperature and water salinity from the CMEMS with a spatial resolution of 0.08° and a time interval of 6 hours.
Time step	From 15 August 2024 to 10 September 2024, with the internal time step of 0.1 second and an internal-external mode split ratio of 10; Output time interval is 1 hour.
Sponge layer	Damping coefficient is 0.1 s^{-1}
Spin-up duration	5 days

computational efficiency for open-ocean simulations (Bi et al., 2015). In contrast, SWAN utilizes a triangular grid, making it particularly suitable for coastal applications (Shao et al., 2024b). Coupling FVCOM with SWAN yields valuable insights into complex wave-current-thermal interactions, including sea surface temperature (SST) cooling during TCs (Wang et al., 2023), turbulent mixing induced by wave breaking (Zheng et al., 2017), and storm surge dynamics (Weisberg and Zheng, 2008).

The dynamical and thermal responses of the ocean to TCs are complex, such as near-internal waves and SST cooling. As a TC induces waves, upwelling, and Ekman transport in the upper ocean, it alters the properties of the mixing layer through vertical entrainment, ocean currents, and pre-existing mesoscale eddies (Wu et al., 2020). These ocean responses can sometimes occur in the deep ocean (Morozov and Velarde, 2008). Previous studies have shown that wave-current interactions are strong during a TC (Chen et al., 2019). Ocean response to TCs varies markedly with intensity and translation speed, especially in shallow waters (Yang et al., 2019). Super typhoons induce particularly complex responses to intense winds (Lin et al., 2009; Mei and Pasquero, 2013; Guan et al., 2024; Liu et al., 2025).

In this study, sea surface dynamics, including currents, sea levels, and waves, are simulated by coupling FVCOM and SWAN, which share a unique triangular grid, to investigate the influences of currents and sea levels on wave simulation. The distinctive contribution of this work is the comprehensive analysis of both wave field characteristics and SST cooling dynamics induced by multiple Super Typhoons transiting the South China Sea basin. The rest of this paper is structured as follows: Section 2 describes the dataset; the methodology, including the reconstruction of typhoon wind and the settings of FVCOM and SWAN, is presented in Section 3; Section 4 presents the results; the oceanic response to Super Typhoon is discussed in Section 5; and the conclusions are given in Section 6.

2. Dataset

The maximum wind speed of Super Typhoon Yagi (2024) upon landing in Hainan Province, China, reached 62 m/s, making it the second strongest typhoon on record in China. The dataset is divided into two portions: the forcing field and open boundary conditions in numerical models, and the measurements from altimeters and moored buoys, which are used to validate the simulated results during Super Typhoon Yagi (2024).

2.1 Forcing field and open conditions

Based on atmospheric numerical models (i.e., the Weather Research and Forecasting Model (WRF)), several agencies officially release wind reanalysis and forecasts, such as the European Centre for Medium-Range Weather Forecasts (ECMWF) (Balmaseda et al., 2008) and the National Centers for Environmental Prediction (NCEP). These wind datasets find extensive application in oceanographic research, including investigations of air-sea interactions during TCs (Foli et al., 2022) and calibration of Synthetic aperture radar (SAR) measurements (Hersbach, 2010). Nevertheless, a well-documented constraint of reanalysis products is their consistent underestimation of peak wind speeds under extreme TC conditions (Stopa and Cheung, 2014). In recent studies (Li et al., 2022; Lai et al., 2023), a practi-

cal approach has been proposed to reconstruct TC winds based on ECMWF reanalysis and the best-track data of a TC. Therefore, ECMWF reanalysis wind data, at 1-hour intervals and with a 0.25 grid resolution, serve as the background source for reconstructing cyclonic wind during Super Typhoon Yagi (2024). For example, the ECMWF wind map at 00:00 UTC on September 4, 2024, is shown in Figure 1a. The triangular grid of the computational region, overlaid with water depth data from the General Bathymetric Chart of the Oceans (GEBCO), is shown in Figure 1b. The figure shows the best tracks of Yagi (2023, red; Shanghai Meteorological Bureau), Doksuri (green), Saola (magenta), Koinu (black), and Haikui (blue) from https://tf.istrongcloud.com. See Table 1 for typhoon characteristics.

Currently, the Copernicus Marine Environment Monitoring Service (CMEMS) provides operational products at 6-hour intervals and with a spatial resolution of 0.08 degrees. In addition to the reconstructed cyclonic wind as the forcing field, the CMEMS reanalysis dataset, known as Global Ocean Physics Analysis and Forecast, which includes water temperature, salinity, and currents, is treated as the open boundary conditions in FVCOM, ensuring heat and energy exchange between the computational and outer regions. Figure 2 shows three maps from the CMEMS dataset at 00:00 UTC on 4 September 2024: a) sea surface temperature, b) sea surface salinity, and c) sea surface current speed.

2.2 Validation dataset

Until now, remotely sensed wind and wave products have been routinely accessible to public researchers with a 1-day delay. The measurements from the Haiyang-2 (HY-2) altimeter, processed into geophysical data records (GDRs), are collected to validate the SWAN-simulated significant wave heights (SWHs). Figure 3a shows the SWH map from the HY-2 altimeter, which was acquired on 4 September 2024. While open-access moored buoy observations in the China Seas are limited, five strategically positioned mooring buoys (MF12001, MF13002, MF14003, MF14006, and MF14007) in the South China Sea (19°N–21°N, 108°E–119°E) provide valuable data for this study. These buoys collect wind speed, current velocity, and wave parameters at 30-minute intervals, offering high-resolution validation data during Super Typhoon Yagi (2024). Figure 3b shows their locations (black triangles), which were used to validate wind and current data, along with Argo locations (red triangles) for water temperature validation.

3. Methodology

This section describes the TC wind field reconstruction methodology, followed by the configuration details for both FVCOM and SWAN models. The two models employ a unidirectional coupling scheme, where FVCOM-simulated current and sea levels serve as direct inputs to SWAN without requiring spatial interpolation, as both models share identical mesh grids.

3.1 TC wind reconstruction

To overcome the limitations of the ECMWF reanalysis data for TCs and further improve the accuracy of the model results, an effective reconstruction method proposed in a previous study (Li et al., 2022) was used in this study, which utilizes the maximum wind speed and the radius of the maximum wind speed of a TC.

The center of the TC is identified according to the best track provided by the Shanghai Meteorological Bureau, which also includes the maximum wind speed and the radius of the maximum wind speed of the TC, denoted as $Maxwind_{SMB}$ and R_{max}, respectively. The wind profile is reconstructed based on the background wind fields

Table 3. Settings for the Simulating WAves Nearshore (SWAN) model.

Forcing filed	ECMWF-based reconstructed wind with a spatial resolution of 0.25° and a time interval of 1 hour.
Frequency bins	Logarithmic, between 0.01 and 1, at intervals of $\Delta f/f = 0.903$.
Resolution	The unstructured grid consists of 56632 computational nodes and 107082 triangular grids with the finest grid resolution of 51.615 m in the South China Sea with a 1-hour temporal resolution.
Bulk formula	Including the white capping induced by the high wind speed.
Directional resolution	10° grid ranged from 0° to 360°.
Propagation scheme	WESTHuysen (non-linear saturation-based white-capping combined with wind).
Bottom friction	JONSWAP with a constant friction coefficient.
Other settings	Wave interaction (QUADrupl); triad wave-wave interactions (TRIad).

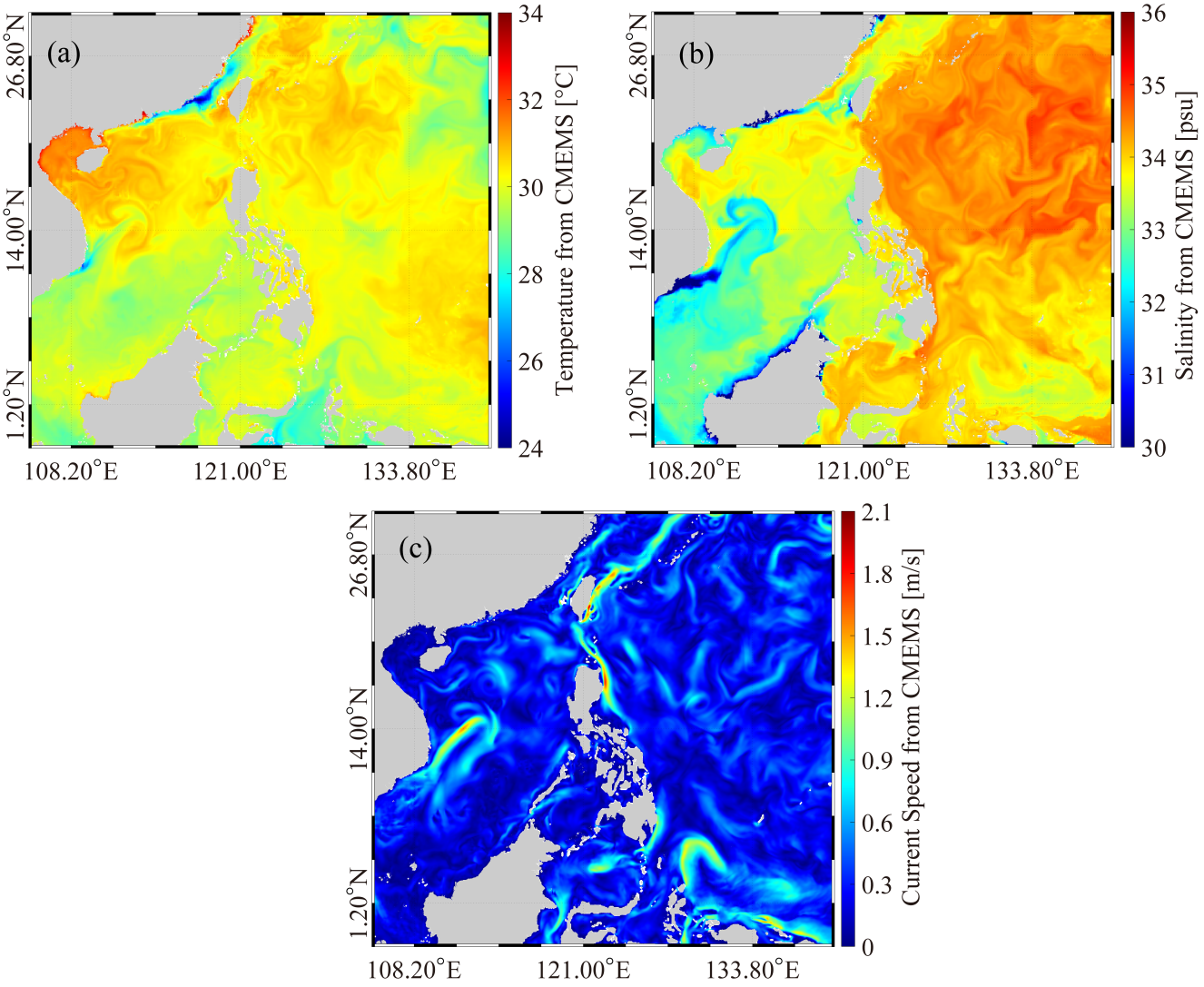

Figure 2. Three maps from the Copernicus Marine Environment Monitoring Service (CMEMS) dataset at 00:00 UTC on 4 September 2024, i.e., sea surface temperature (a), sea surface salinity (b) , and sea surface current speed (c).

provided by the ECMWF reanalysis data, denoted as U_{10}. The maximum wind speed of the TC, calculated from the ECMWF reanalysis data, is denoted as $Maxwind_{EC}$. In addition to the above parameters, the reconstruction method is also determined by the distance correction parameter r from the TC's eye, as shown in the following equations:

$$V_r = \begin{cases} \left(\frac{r}{R_{max}} Ratio + \frac{R_{max}-r}{R_{max}}\right) U_{10} \\ \qquad\qquad 0 \le r < R_{max} \\ \left[\frac{r-R_{max}}{nR_{max}} Ratio + \frac{(n-1)R_{max}-r}{nR_{max}} Ratio\right] U_{10} \\ \qquad\qquad R_{max} \le r < n\,R_{max}, n \ge 2 \end{cases} \quad (1)$$

where

$$Ratio = \frac{Maxwind_{SMB}}{Maxwind_{EC}} \quad (2)$$

Figure 4a shows the map for Super Typhoon Yagi (2024) at 00:00 UTC on 4 September 2024, obtained using the reconstruction method. Compared to Figure 1a, it is clear that the intensity of the reconstructed wind is higher than that of the ECMWF wind. The maximum wind speed obtained using the reconstruction method reached 30 m/s, while the maximum wind speed from the ECMWF only reached 20 m/s. A comparison of wind speeds up to 40 m/s between the reconstruction and available buoys is shown in Figure 4b, yielding a root mean squared error (RMSE) of 4.01 m/s, a Pearson correlation coefficient (Cor) of 0.90,

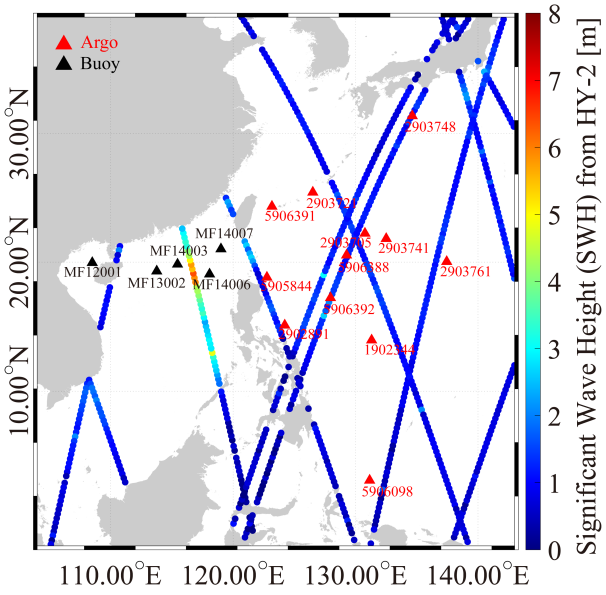

Figure 3. Significant wave height (SWH) map from Haiyang-2 (HY-2) altimeter acquired on 4 September 2024.

and a scatter index (SI) of 0.48. This result indicates the applicability of the reconstructed TC wind for simulation by FVCOM and SWAN.

3.2 Settings of FVCOM

FVCOM employs an unstructured grid, providing flexibility in modeling complex coastlines and shallow water areas (Chen et al., 2003). It employs a finite-volume approach, allowing for high spatial resolution over complex topographies, and has been widely used for simulating oceanographic and coastal processes. The model contains both Cartesian and spherical coordinates. In the horizontal direction, the discrete method is based on triangular grids, and the turbulence closure is the Mellor and Yamada (Mellor and Yamada, 1982) level 2.5 (MY-2.5) scheme. In the vertical direction, the discrete method employs a generalized terrain-following coordinate system, which includes the commonly used sigma coordinates. The turbulence closure is based on the Smagorinsky scheme. FVCOM includes a wet-or-dry treatment, making it suitable for large tidal flat areas. The basic governing equations of FVCOM are shown below, including the momentum, continuity, temperature, salinity, and density equations:

$$\frac{\partial u}{\partial t}+u\frac{\partial u}{\partial x}+v\frac{\partial u}{\partial y}+w\frac{\partial u}{\partial z}-f_v= -\frac{1}{\rho}+\frac{\partial(p_H+p_a)}{\partial x}-\frac{1}{\rho}\frac{\partial q}{\partial x}+\frac{\partial\left(K_m\frac{\partial u}{\partial z}\right)}{\partial z}+F_u \tag{3}$$

$$\frac{\partial v}{\partial t}+u\frac{\partial v}{\partial x}+v\frac{\partial v}{\partial y}+w\frac{\partial v}{\partial z}+f_u= -\frac{1}{\rho}+\frac{\partial(p_H+p_a)}{\partial y}-\frac{1}{\rho}\frac{\partial q}{\partial y}+\frac{\partial\left(K_m\frac{\partial v}{\partial z}\right)}{\partial z}+F_v \tag{4}$$

$$\frac{\partial w}{\partial t}+u\frac{\partial w}{\partial x}+v\frac{\partial w}{\partial y}+w\frac{\partial w}{\partial z}=\frac{-1}{\rho}\frac{\partial q}{\partial y}+ +\frac{\partial\left(K_m\frac{\partial w}{\partial z}\right)}{\partial z}+F_w \tag{5}$$

$$\frac{\partial u}{\partial x}+\frac{\partial v}{\partial y}+\frac{\partial w}{\partial z}=0 \tag{6}$$

$$\frac{\partial T}{\partial t}+u\frac{\partial T}{\partial x}+v\frac{\partial T}{\partial y}+\frac{\partial T}{\partial z}=\frac{\partial\left(K_h\frac{\partial T}{\partial z}\right)}{\partial z}+F_T \tag{7}$$

$$\frac{\partial S}{\partial t}+u\frac{\partial S}{\partial x}+v\frac{\partial S}{\partial y}+\frac{\partial S}{\partial z}=\frac{\partial\left(K_h\frac{\partial S}{\partial z}\right)}{\partial z}+F_S \tag{8}$$

$$\rho=\rho(T,S,P) \tag{9}$$

where x, y, and z are the east, north, and vertical axes in the Cartesian coordinate system, respectively; u, v, and w are the velocity components in the x, y, and z directions, respectively; T is the sea temperature; S is the salinity; ρ is the sea-water density; p_a is the air pressure at the sea surface; p_H is the hydrostatic pressure; q is the non-hydrostatic pressure; f is the Coriolis parameter; g is the acceleration of gravity; K_m is the vertical eddy viscosity coefficient; and K_h is the thermal vertical eddy diffusion coefficient. F_u, F_v, and F_w represent the horizontal momentum in the x, y and vertical z direction, respectively; F_T and F_S represent the thermal and salt diffusion terms, respectively. Noted that changes in water temperature and surface salinity due to turbulent (i.e., sensible and latent) heat fluxes are not considered here.

This study utilizes ECMWF-based reconstructed winds as the atmospheric forcing field. Tidal forcing is incorporated using the TPXO.7 tidal model, which provides high-resolution harmonic constants for eight principal tidal constituents (M2, S2, N2, K2, K1, O1, P1, and Q1). The TPXO.7 dataset is widely regarded for its accurate representation of tidal dynamics. Water temperature, salinity, surface

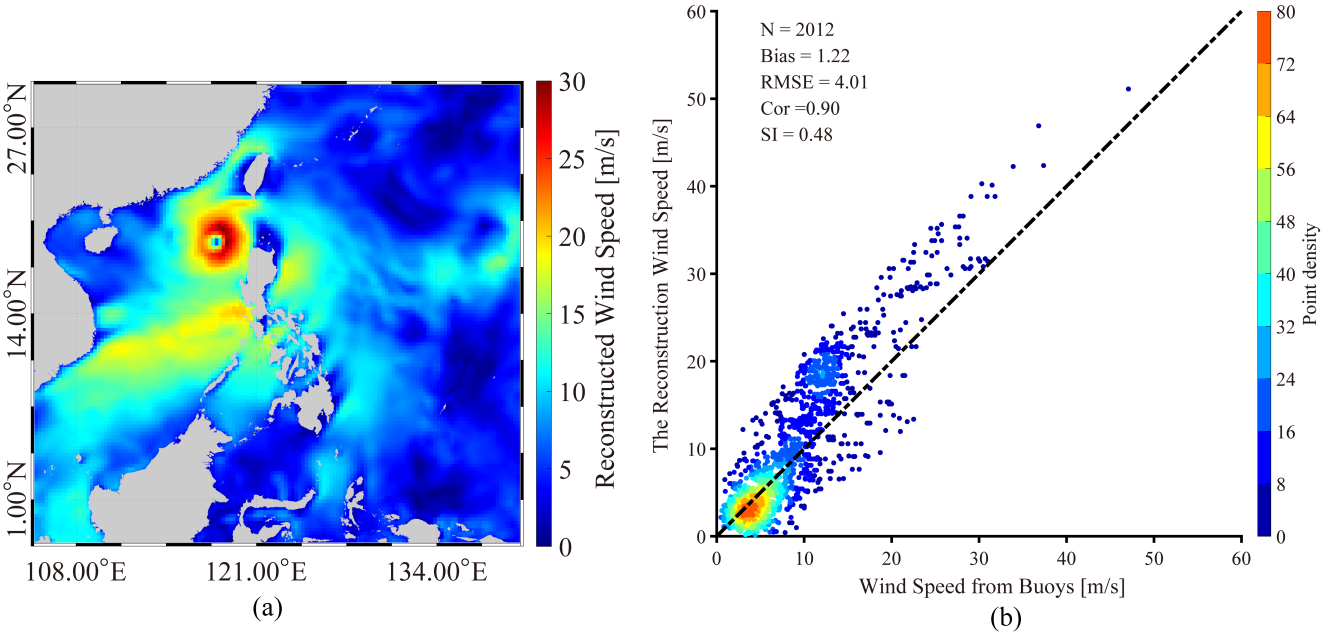

Figure 4. Wind map during Super Typhoon Yagi (2024) at 00:00 UTC on 4 September 2024 obtained using the reconstruction method (a). Comparison of wind speed between reconstruction results and five moored buoys (b).

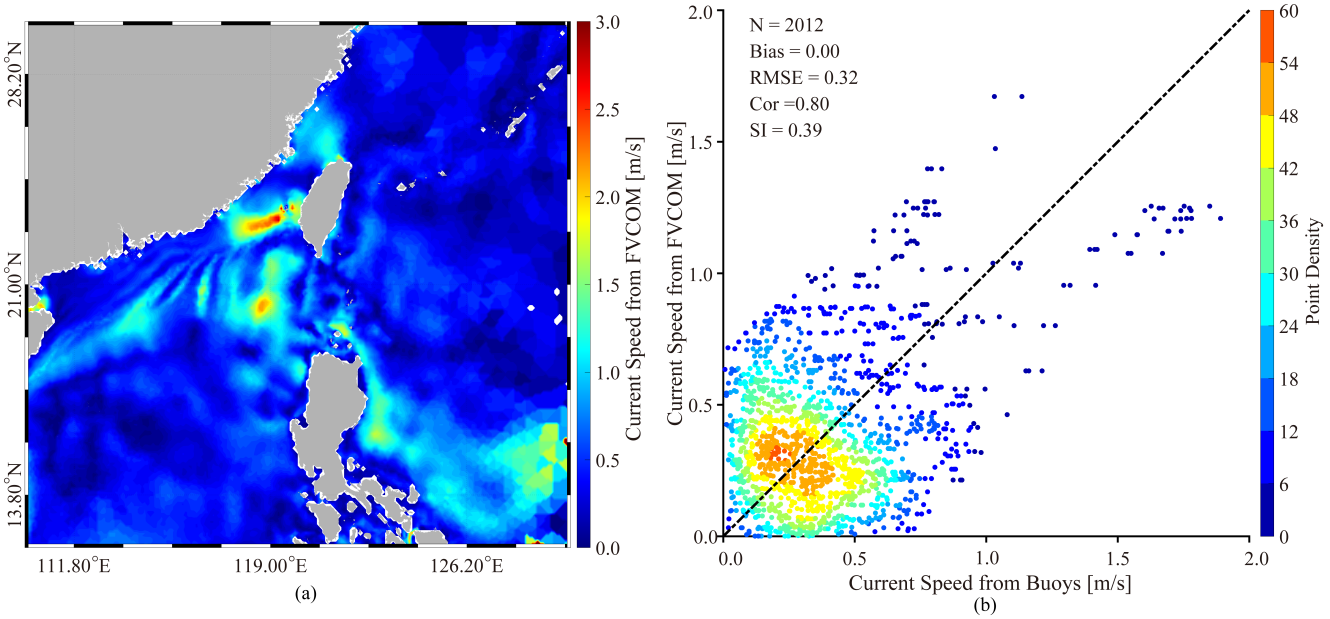

Figure 5. Current speed map from the Finite-Volume Community Ocean Model (FVCOM) during Super Typhoon Yagi (2024) at 00:00 UTC on 4 September 2024 (a). Comparison of current speed between reconstruction and five moored buoys (b).

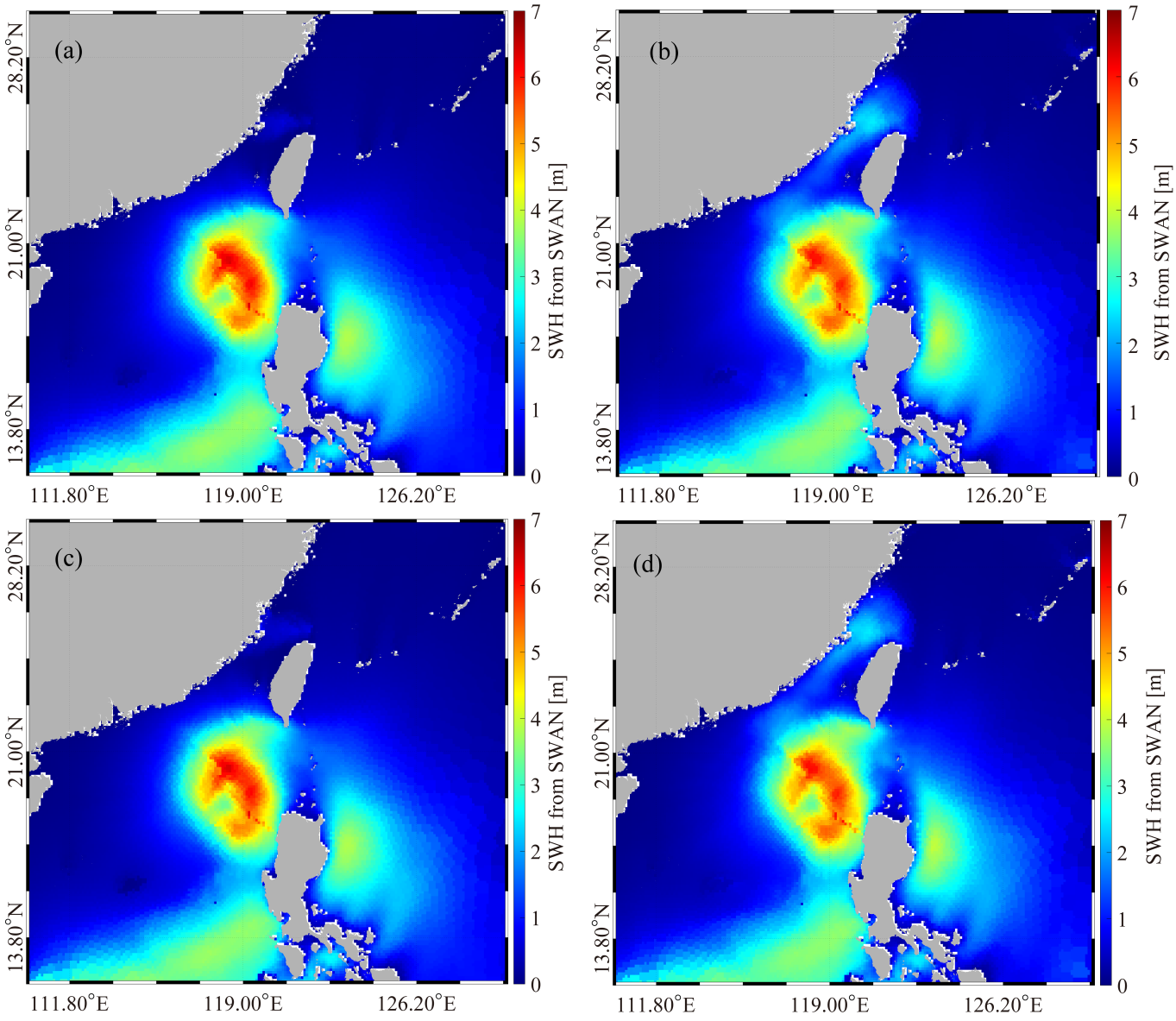

Figure 6. Simulated wave height distribution by Simulating WAves Nearshore (SWAN) which are acquired at 00:00 UTC on 4 September 2024, i.e., using reconstructed TC wind, b) using reconstructed TC wind and current (a), using reconstructed TC wind and sea level (c), and using reconstructed TC wind, current, and sea level (d).

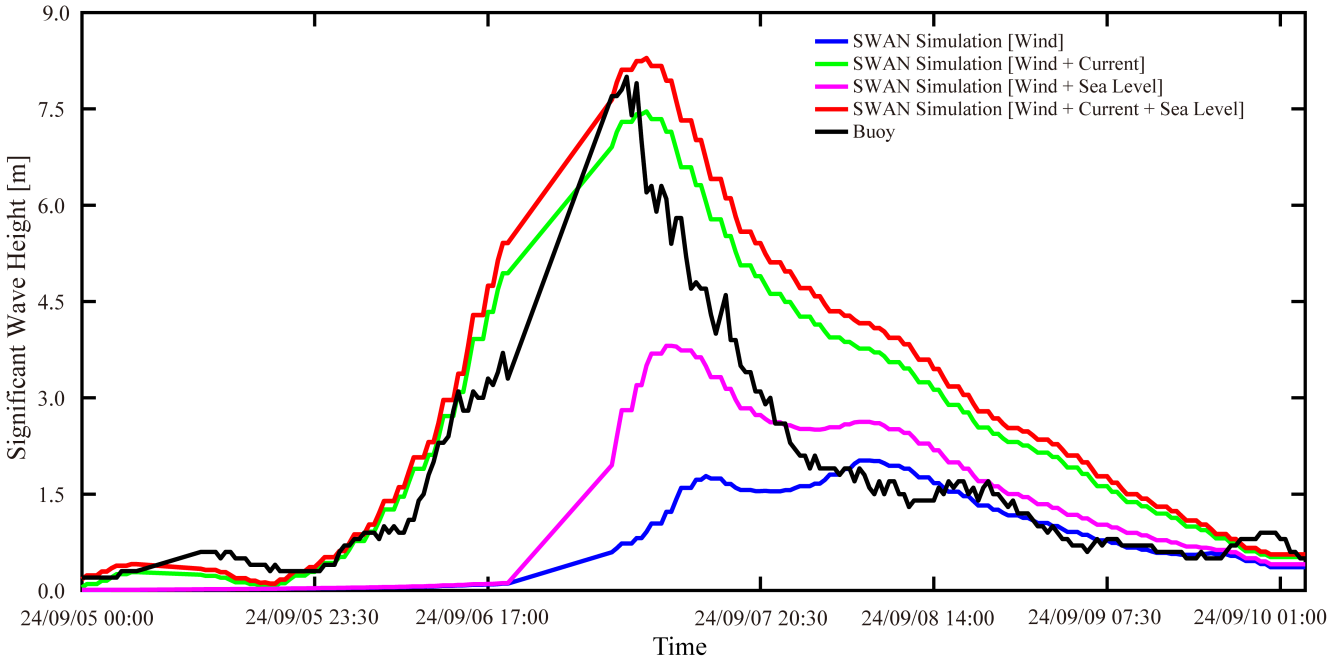

Figure 7. Time series of SWH located at buoy MF14007.

elevation, and current velocity data from CMEMS were also employed to define the open boundary conditions. A sponge layer was specified around this area, featuring a damping zone that transitions from the open boundary into the interior, with a specified influence radius. Additionally, the damping coefficient is set to 0.1 s^{-1}. The water temperature and salinity data from CMEMS were also used as the initial field. To ensure the stability of FVCOM, the simulation was run from August 15, 2024, to September 10, 2024. The typical spin-up period ranges from 2 to 5 days; a 5-day duration is implemented in this study to ensure model stability. The largest grid of the mesh covers 105°E–140°E and 1°S–36°N. The detailed FVCOM model settings are briefly presented in Table 1.

3.3 Settings of SWAN

The SWAN model, a third-generation fully spectral model, enables realistic simulations of wave parameters for coastal areas, lakes, and estuaries, based on specified wind, bottom friction, and current conditions (Booij et al., 1999). It uses the action density $N(\sigma,\theta)$ to calculate the development of a sea state, which is more conserved than the variance density. θ is the wave propagation direction, and σ is the relative frequency. The spectral action balance equation describes the evolution of the wave spectrum. Based on the spectral action balance equation, the governing equation of the SWAN model, considering ambient current, is written in Cartesian coordinates as follows:

$$\frac{\partial_N}{\partial_t} + \Delta \times [(C_g + V)N] + \frac{\partial C_\sigma N}{\partial_\sigma} + \frac{\partial C_\theta N}{\partial_\theta} = \frac{S_t}{\sigma} \quad (10)$$

in which t is the time; C_σ and C_θ are the wave propagation velocities in terms of the spectral space σ and θ, respectively; C_g is the group velocity vector; V is the sea-surface current vector; and Δ is the Hamiltonian divergence operator. S_t comprises the input and dissipation source terms, stated as follows:

$$S_t = S_{in} + S_{bot} + S_{nl} + S_{tq} + S_{db} \quad (11)$$

wherein S_{in} represents the effect of the atmosphere–wave interaction; S_{bot} is the friction induced by wave–bottom interaction; S_{nl} is the nonlinear wave–wave interaction term; S_{tq} represents the three-wave (triad) and four-wave (quadruplet) components of the wave–wave interactions; and S_{db} is the wave decay due to white capping and depth-induced wave breaking. The detailed SWAN model settings are briefly presented in Table 2.

The sea surface roughness z_0 had been parameterized based on data recorded by buoys, towers, and ships. Charnock (1955) proposed a now well-known formula to estimate the sea surface roughness:

$$\frac{g z_0}{u_*^2} = \alpha \quad (12)$$

in which g is the gravitational acceleration; α is a universal constant (e.g., $\alpha = 0.0185$ by Wu (1982); and u_* is the wind friction velocity related to the wind speed U_{10}.

The vertical profile of wind speed with respect to height is given as follows:

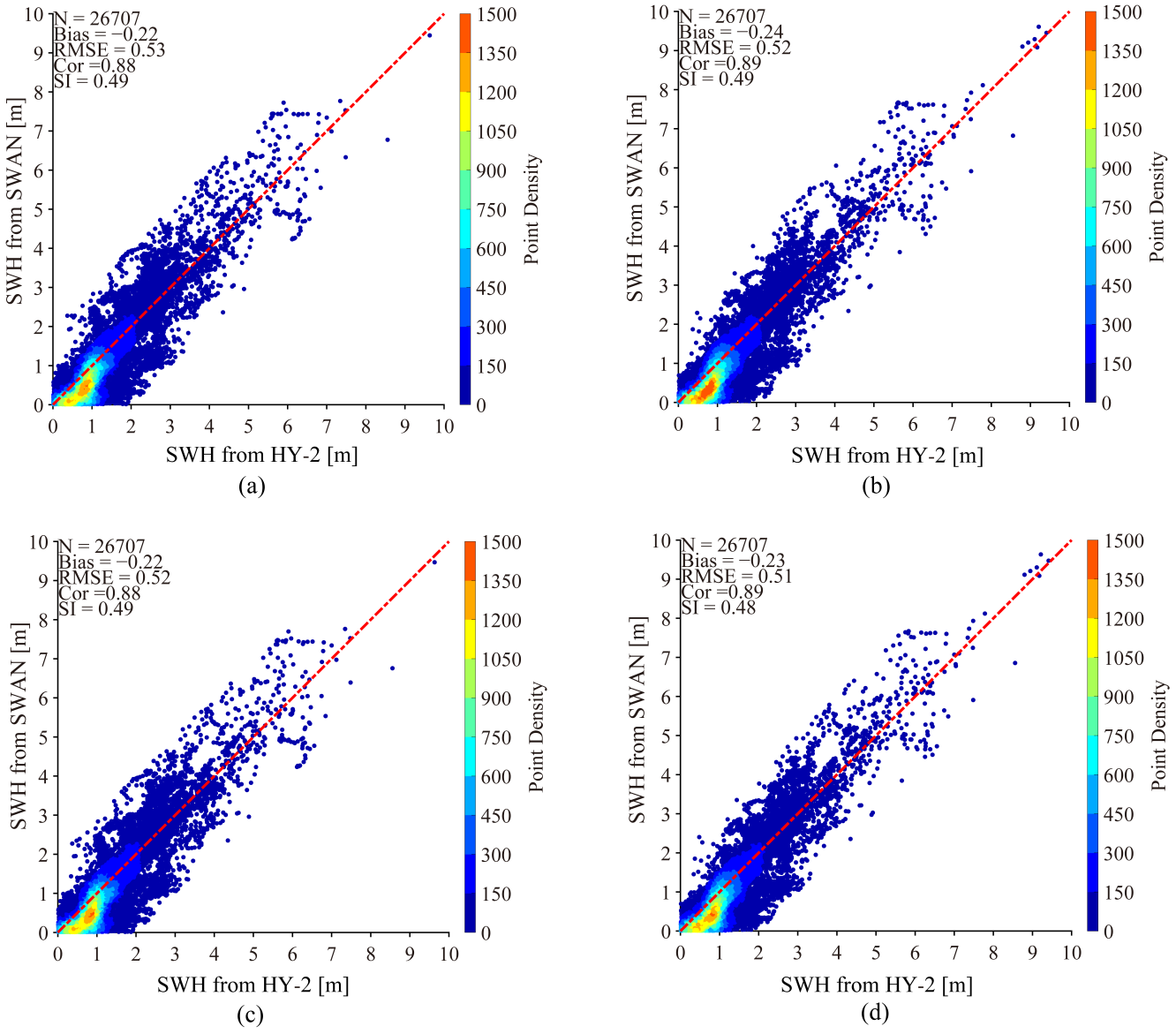

Figure 8. Comparison of simulated SWHs with the measurements from HY-2 altimeter, i.e., using reconstructed TC wind (a), using reconstructed TC wind and current (b), using reconstructed TC wind and sea level (c), and using reconstructed TC wind, current, and sea level (d).

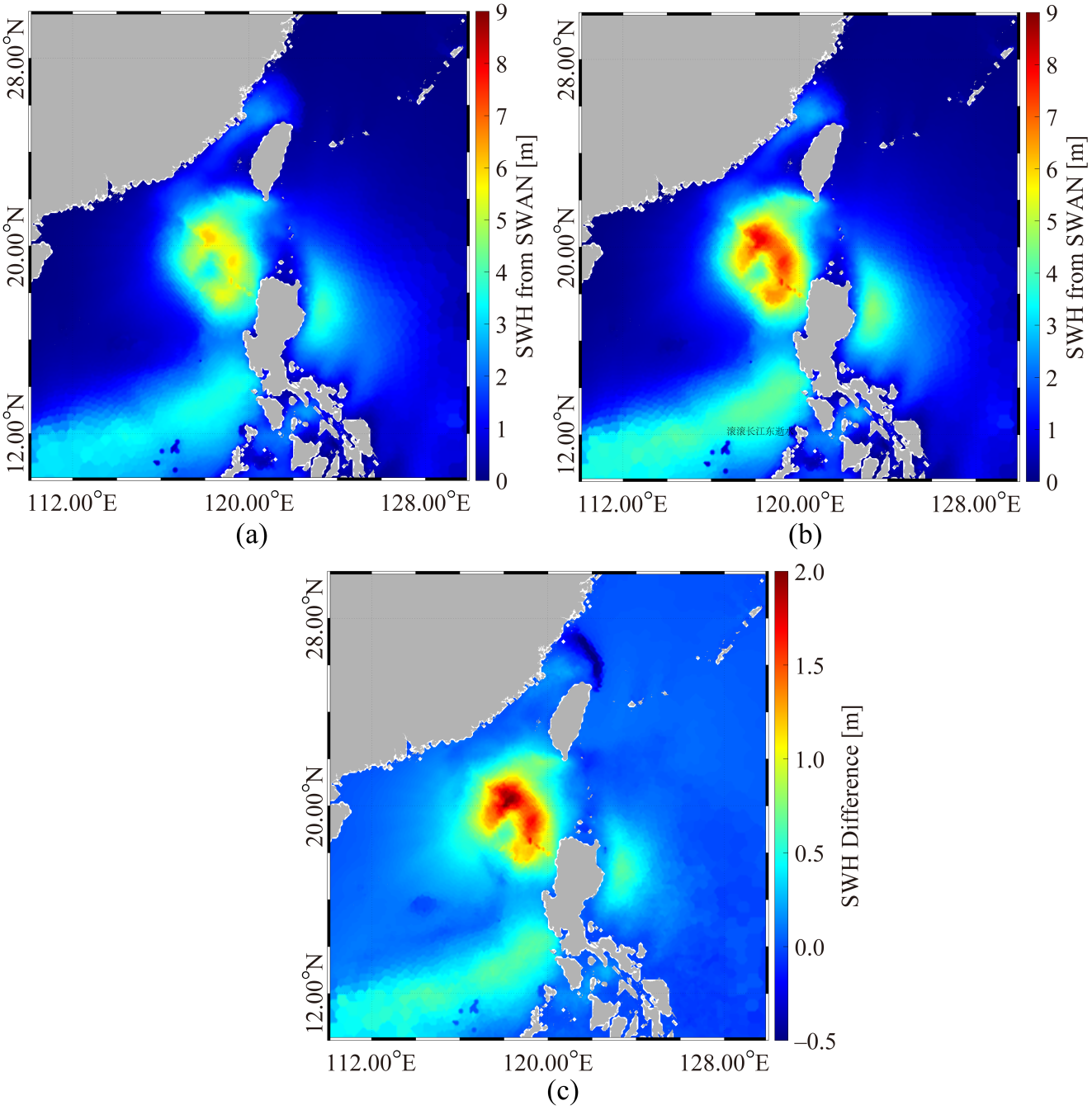

Figure 9. SWH distributions at 00:00 UTC on 4 September 2024 simulated using two drag coefficient (C_d) parameterizations: Wu (1982) scheme (a), Hu et al. (2024) scheme (b), and their SWH differences (c).

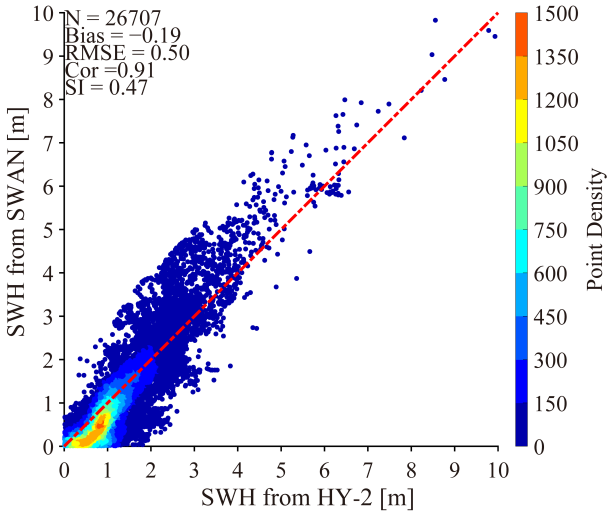

Figure 10. Validation of SWAN-simulated SWHs using parameterization by Hu et al. (2024) against the measurements from HY-2 altimeter during collected TCs.

$$u_{10} = \frac{u_*}{\kappa} ln\left(\frac{10}{z_0}\right) \tag{13}$$

in which the von Karman velocity κ is 0.40. The roughness length and neutral drag coefficient at 10 m are then related as follows (Vickers et al., 2013):

$$C_d = \left[\frac{\kappa}{ln\left(\frac{10}{z_0}\right)}\right]^2 \tag{14}$$

The original drag coefficient used in the SWAN model was given by Wu (1982) as follows:

$$C_d = 0.8 + 0.065U_{10} \tag{15}$$

In recent study (Hu et al., 2024) a new wind drag parameterization considering the impact of sea state on sea roughness z_0 (Eq. (14)) is proposed, which is adopted using wave spectrum measured by SWIM collocated with high wind from radiometer:

$$C_d \times 10^3 = C_0 + C_1U_{10} + C_2U_{10}^2 + C_3U_{10}^3 + C_4U_{10}^4 \tag{16}$$

in which the constants A–E are fitted based on a combination of laboratory and field data, i.e., $C_0 = 104.2$, $C_1 = -12.37$, $C_2 = 2.415$, $C_3 = -0.07996$, and $C_4 = 0.0007891$. The above formula depends solely on the wind speed and can be applied in practice in the modelling process by employing the input/dissipation source terms. The schemes selected in SWAN are listed in Table 3.

4. Results

In this section, the influence of FVCOM-simulated sea surface currents and sea level on wave simulation by SWAN is analyzed. Then, the performance of the previous and updated parameterizations of the drag coefficient C_d used in SWAN is studied.

4.1 Influence of sea surface current and sea level

To validate the FVCOM simulations, the modeled sea surface current speeds are compared with observations from five moored buoys. Figure 5a shows the FVCOM-simulated sea surface current speed map at 00:00 UTC on 4 September 2024, where the current speed reaches up to 2 m/s. A statistical analysis of the current speed is presented in Figure 5b, yielding a 0.32 m/s RMSE, a 0.80 correlation (Cor), and a 0.39 scatter index (SI). Based on these results, it is concluded that the FVCOM simulation is reliable for hindcasting waves using SWAN.

Considering various open boundary conditions, the SWAN-simulated SWH maps at 00:00 UTC on 4 September 2024 are shown in Figure 6 a) using reconstructed TC wind, b) using reconstructed TC wind and current, c) using reconstructed TC wind and sea level, and d) using reconstructed TC wind, current, and sea level. It is clearly observed that the difference to the west of Taiwan Island is significant when the influence of the current is taken into account. Figure 7 presents a time series of SWH at buoy MF14007, where the variation in SWH influenced by current closely matches the measurements from the buoy.

Figure 8 compares the simulated SWHs with measurements from the HY-2 altimeter: a) using reconstructed TC wind, b) using reconstructed TC wind and current, c) using reconstructed TC wind and sea level, and d) using reconstructed TC wind, current, and sea level. It is found that the accuracy of SWHs up to 10 m is highest (i.e., a 0.51 m RMSE, 0.89 Cor, and a 0.48 (SI) compared to the other results. The observed overestimation in HY-2 products for SWH below 1 m is likely attributable to the coarse spatial resolution (10 km) of the altimeter in coastal waters.

4.2 Performance of previous and updated C_d

The C_d parameterization is essential in hindcasting waves using numerical wave models, especially under extreme weather conditions. In our previous study, the C_d parameterization in WW3 was improved based on remotely sensed products during TCs. Here, the performance of the C_d parameterization in SWAN is investigated, considering recon-

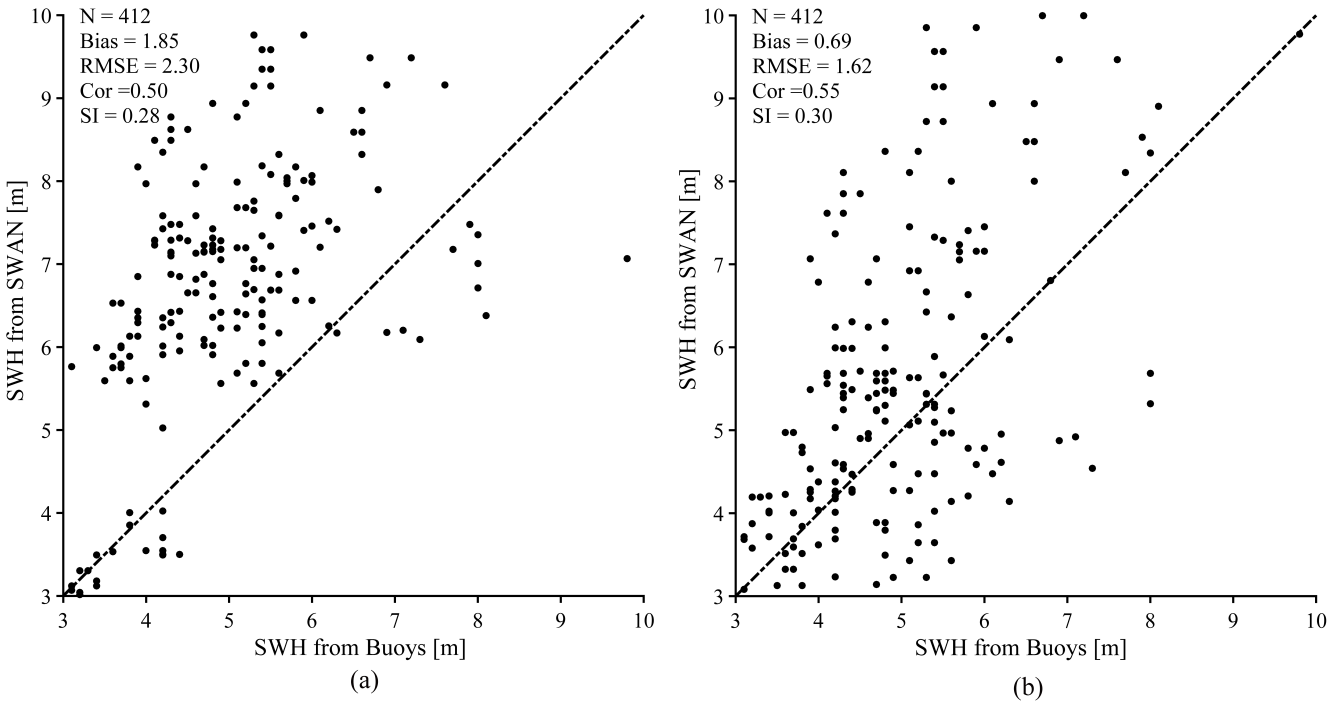

Figure 11. Validation of SWAN-simulated SWHs against the measurements from buoys at SWH > 3 m, i.e., parameterization of C_d by Wu (1982) (a) and parameterization of C_d by Hu et al. (2024) (b).

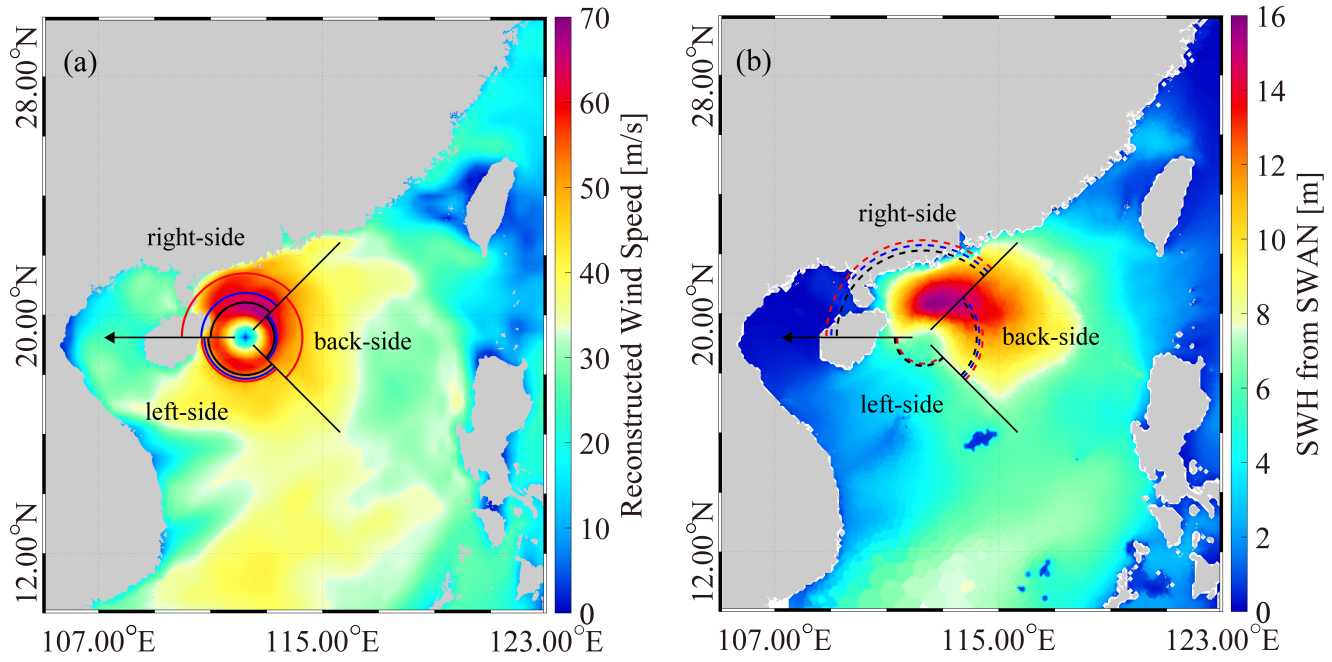

Figure 12. Two maps at 09:06 UTC on 4 September 2024 during Super Typhoon Yagi (2024) landfall on Hainan Island, China: wind field (a) and SWH (b). The red, blue, and black solid/dashed lines indicate wind/SWH radii for 30 m/s (R30, 4.5 m), 40 m/s (R40, 6 m), and 50 m/s (R50, 7.5 m), respectively.

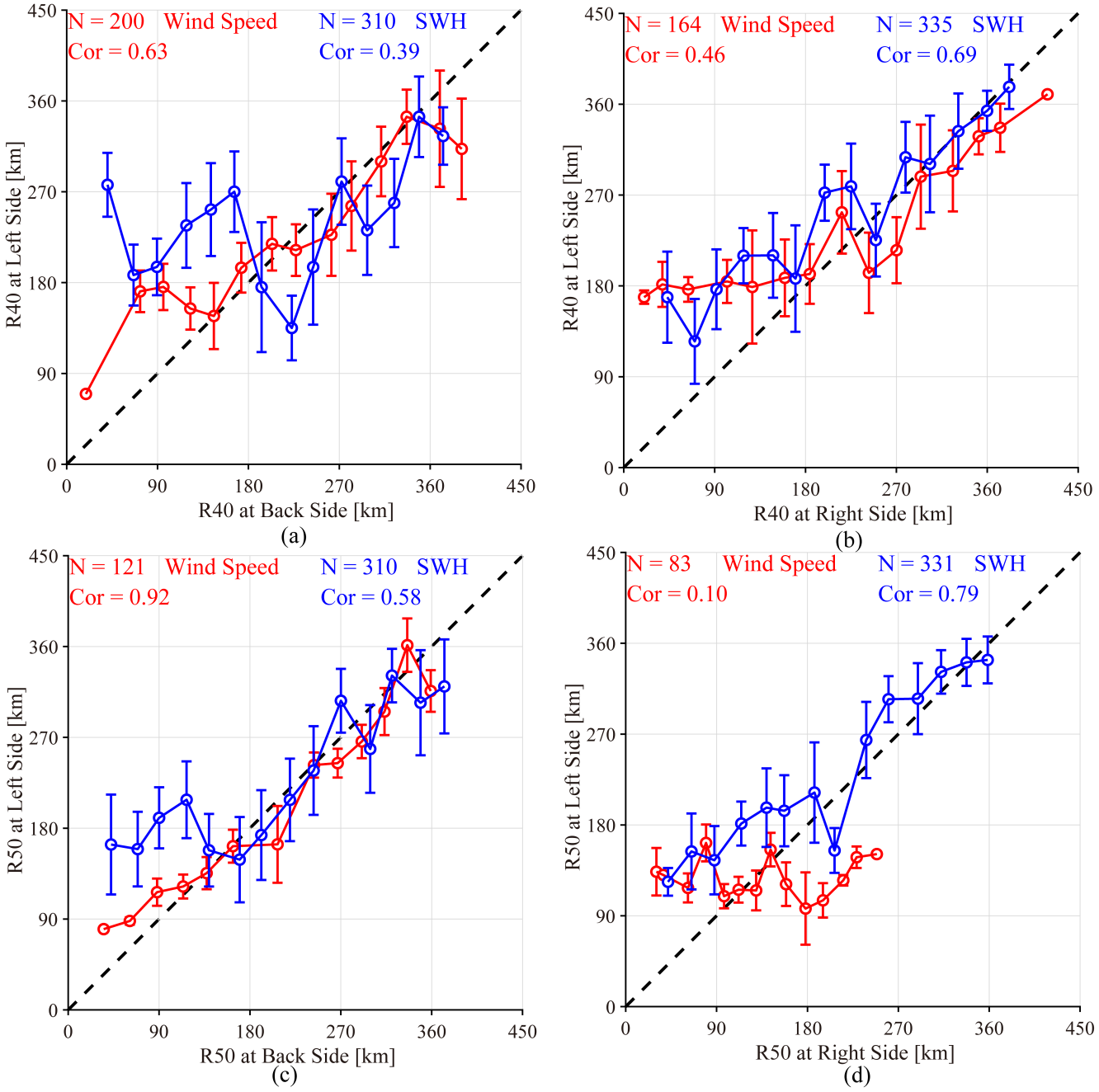

Figure 13. Relationships between wind radii and SWH at different sectors of TC using errorbars: R40 (a)–(b) and R50 (c)–(d). 40 m/s, and N is the number of available samples.

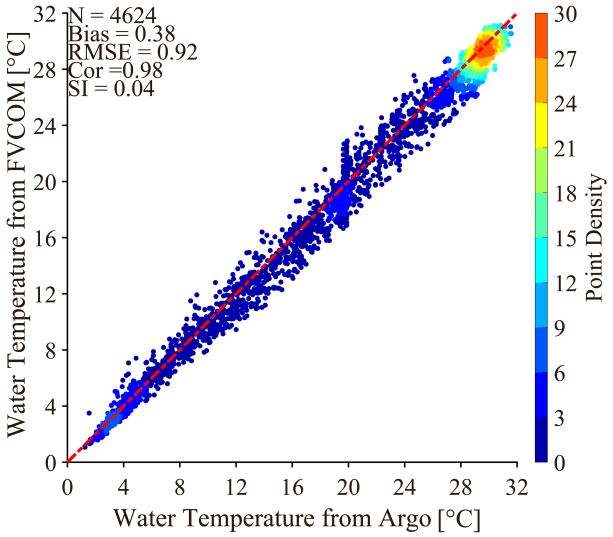

Figure 14. Comparison of water temperature between FVCOM simulations and Argo observations.

structed TC wind, current, and sea level. Figure 9 presents SWH distributions at 00:00 UTC on 4 September 2024 simulated using two C_d parameterizations: a) the Wu (1982) model, b) the Hu et al. (2024) model, and c) their SWH differences. Notably, substantial SWH discrepancies occur near the typhoon eye when comparing both parameterizations. Validation against HY-2 altimeter measurements during five super typhoons reveals the Hu model achieves an RMSE of 0.50 m, Cor of 0.91, and SI of 0.47 (Figure 10). In particular, the performance of the Hu model is better for SWHs $>$ 4 m. Therefore, validation against measurements from buoys during Super Typhoon Yagi (2024) for SWHs $>$ 3 m is presented in Figure 11. Clearly, the error in the SWAN-simulated SWH has decreased by 0.6 m when using the Hu model, particularly improving the over-estimation. However, it is noted that the applicability of C_d still needs to be investigated in other regions.

5. Discussion

It is interesting to discuss the asymmetry of wind and wave and SST cooling during a super typhoon. The well-known parametric wave model, i.e., the E-spectrum (Elfouhaily et al., 1997), is directly employed to estimate the SWHs at various wind speeds, i.e., 30 m/s (R30), 40 m/s (R40), and 50 m/s (R50) of wind radii, corresponding to 4.5 m, 6 m, and 7.5 m of SWH radii, respectively. Figure 12a shows wind conditions at 09:06 UTC on 4 September 2024 during Super Typhoon Yagi (2024) landfall on Hainan Island, China. The plot includes three wind radius contours: red (30 m/s), blue (40 m/s), and black dashed lines (50 m/s), corresponding to the track of the typhoon. Similarly, Figure 12b depicts the SWH map, with the red, blue, and black solid lines representing the 4.5 m, 6 m, and 7.5 m SWH radii, respectively. Figure 13 presents relationships between wind radii and SWH across TC sectors using error bars: (a,b) R40 and (c,d) R50 (where N indicates sample size). Generally, wind and SWH variations show strong consistency, as expected from wind-wave dynamics. However, wind Cor is lower in the right-front quadrant (0.1 due to limited samples) compared to the left-right quadrant, consistent with dominant wind forcing patterns. Conversely, SWH correlations remain relatively high in the right-back quadrant, reflecting swell influence. Both quadrants show increasing SWH correlations with wind speed.

FVCOM-simulated temperatures match Argo observations during typhoons with 0.92°C RMSE, 0.98 Cor, and 0.04 SI (Figure 14), demonstrating model reliability. Figure 15 shows $>$ 50 m/s wind SST differences for: a) Haikui (September 3–2, 2023), b) Doksuri (July 25–24, 2023), c) Yagi (September 6–5, 2024), d) Saola (August 30–29, 2023), and e) Koinu (October 4–3, 2023). The analysis reveals pronounced SST cooling directly over typhoon tracks, with maximum cooling reaching 4°C during Super Typhoon Doksuri (2023). Weaker cooling (1°C) occurs when typhoons interact with warmer waters from the Kuroshio Current (i.e., Haikui and Koinu) and Zhejiang-Fujian Coastal Current (Yagi). This thermal response explains the inverse relationship between the current speed difference and the SST difference, as shown by the red solid line in Figure 16a. Figure 16b demonstrates a positive linear correlation between SST and SWH differences. Under extreme conditions, wave-induced processes (breaking and radiation stress) intensify air-sea heat exchange, amplifying SST cooling.

6. Conclusion

As TCs approach coastal areas, their impacts intensify significantly, generating strong winds, large waves, heavy rainfall, and storm surges. Super typhoons (wind speeds $>$ 51 m/s) represent particularly severe marine hazards for coastal regions. This study examines sea surface dynamics (currents, sea levels, and waves) during five super typhoons following similar tracks: Haikui (2023), Doksuri (2023), Yagi (2024), Saola (2023), and Koinu (2023). Using coupled FVCOM-SWAN modeling, we investigate how currents and sea levels influence wave simulations, with particular focus on wind-wave asymmetry and SST cooling patterns.

Based on the ECMWF reanalysis data at 1-hour intervals and 0.25° grids, the wind field is reconstructed to ensure the availability of typhoon wind data. A comparison of the typhoon wind speed with measurements from five moored buoys shows a 4.01 m/s RMSE, a 0.90 Cor, and a 0.48 SI. Using the typhoon wind and the daily CMEMS dataset (i.e., water temperature, salinity, and current) as the forcing field and open boundary conditions, the sea surface current and sea level are hindcast using FVCOM during five super typhoons. Validation of current speeds

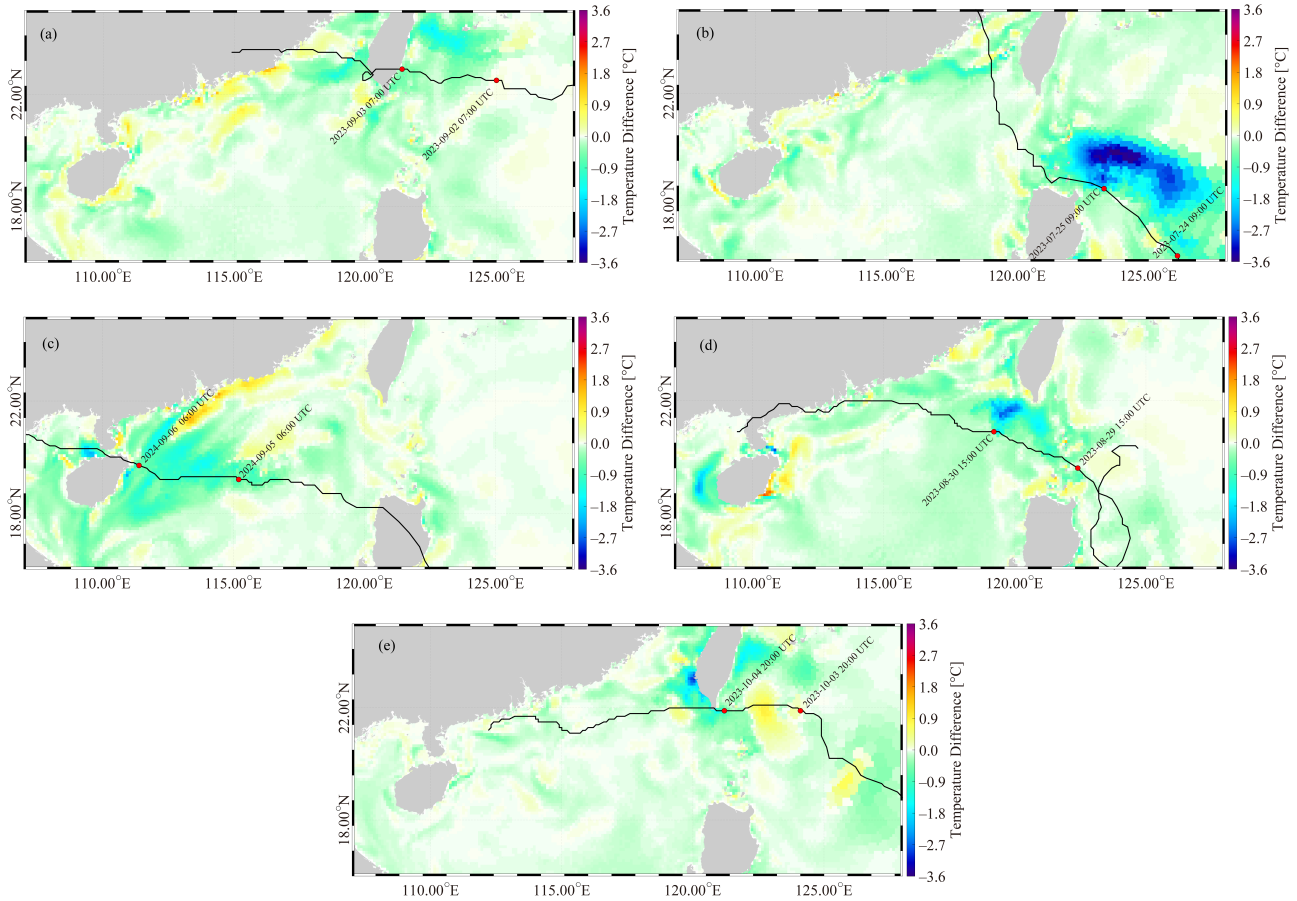

Figure 15. Sea surface temperature (SST) differences during extreme wind conditions (> 50 m/s) for five super typhoons: a) Haikui (3 vs. 2 September 2023), b) Doksuri (25 vs. 24 July 2023), c) Yagi (6 vs. 5 September 2024), d) Saola (30 vs. 29 August 2023), and e) Koinu (4 vs. 3 October 2023).

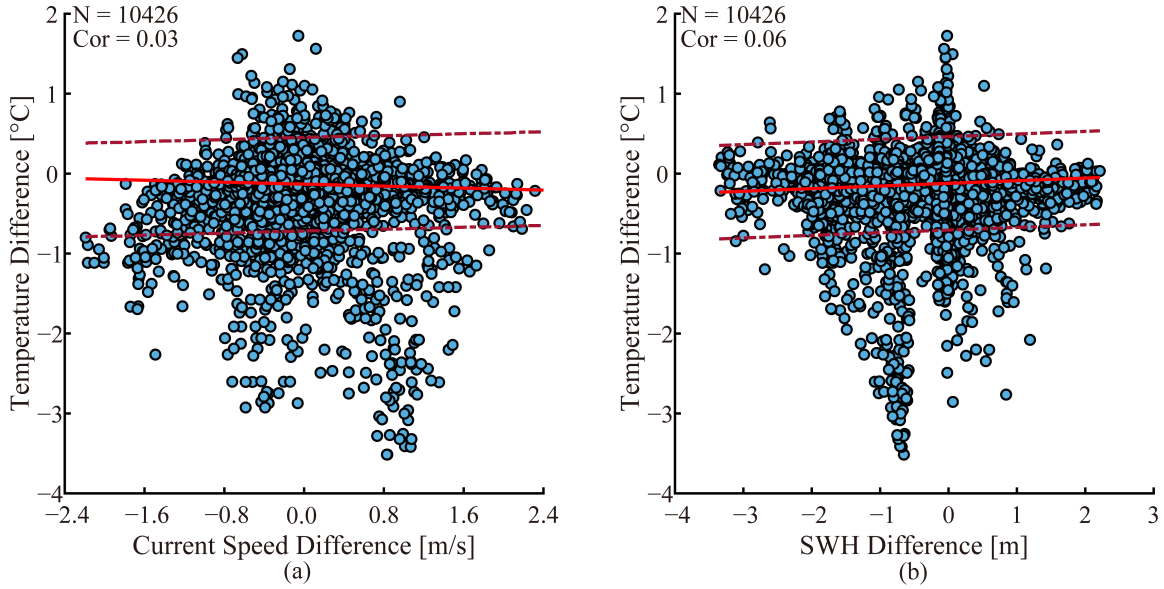

Figure 16. Regression analysis of SST differences against: current speed anomalies (a) and SWH variations (b). The red solid and dotted lines indicate the regression fit and 95% prediction intervals, respectively.

against buoy measurements yields a 0.32 m/s RMSE with a 0.80 Cor and a 0.39 SI. It is found that the accuracy of the SWAN-simulated SWH improves when the influences of current and sea level are included, with a 0.51 m RMSE, 0.89 Cor, and a 0.48 SI, compared to a 0.53 m RMSE, 0.88 Cor, and 0.49 SI when only typhoon wind is used. In this regard, it is concluded that current and sea level should be considered in wave simulations, especially in coastal waters.

SWAN simulations test two drag coefficient (C_d) parameterizations: the Wu (1982) model and the Hu et al. (2024) model. Validation against HY-2 altimeter and buoy data demonstrates the Hu model's superior performance for SWH $>$ 3 m, reducing overestimation by 0.6 m relative to the Wu model. According to the direction of TC movement, the structures of TC wind and waves were divided into three quadrants at several wind clusters, i.e., 30 m/s (R30), 40 m/s (R40), and 50 m/s (R50) wind radii corresponding to 4.5 m, 6 m, and 7.5 m SWH radii. Both variations in wind and SWH radii are consistent in the three quadrants. While wind Cors are higher in the left-right quadrant than in the left-back quadrant, SWH distributions show the opposite trend due to swell influence. Both wind and SWH correlations at the R50 radius exceed those at R40, suggesting increasingly symmetric wind and wave fields under stronger winds. Maximum SST cooling reaches 4°C at wind speeds $>$ 50 m/s during Super Typhoon Doksuri (2023), while the Kuroshio Current and Zhejiang-Fujian Coastal Current limit cooling to just 1°C. Regression analysis further reveals a significant negative relationship between SST anomalies and current speed variations. These findings significantly improve our capacity to predict extreme wave conditions during super typhoons, providing critical support for coastal hazard mitigation and resilient infrastructure planning. Furthermore, the validated optimal drag coefficient parameterization can be operationally implemented in forecasting systems to enhance wave prediction accuracy, particularly in high-risk areas such as the Taiwan Strait.

SAR (Zhou et al., 2022) delivers fine-scale observations (10–40 m resolution) across wide swaths (200–300 km), making it ideal for monitoring TC surface dynamics including winds, waves, currents and rainfall (Shen et al., 2014; Shao et al., 2023, 2024a; Zhou et al., 2024). In the near future, utilizing SAR measurements, the asymmetry of wind and waves during a TC will be further analyzed.

Acknowledgments

We greatly appreciate the Marine Ecosystem Dynamics Modeling Laboratory and Delft University of Technology for providing the original codes of the Finite-Volume Community Ocean Model (FVCOM) and Simulating WAves Nearshore (SWAN), respectively. The reconstructed winds, based on data from the European Centre for Medium-Range Weather Forecasts (ECMWF), and the topographic bathymetry from the General Bathymetric Chart of the Oceans (GEBCO) serve as the forcing field and bottom boundary in FVCOM and SWAN. The open boundary conditions in FVCOM include sea surface temperature, sea surface salinity, sea surface currents, and sea level data from the Copernicus Marine Environment Monitoring Service (CMEMS). Track information for super typhoons is provided by the Shanghai Meteorological Bureau. Measurements from the Haiyang-2 satellite are officially released by the National Satellite Ocean Application Service (NSOAS), and the data from moored buoys are shared by the South China Sea Survey Center, Ministry of Natural Resources.

Conflict of interest

None declared.

Data availability

Data will be made available upon request.

Funding

This work was funded by the National Natural Science Foundation of China under grant 42376174 and the Natural Science Foundation of Shanghai under grant 23ZR1426900.

References

Boutin, J., Etcheto, J., 1990. *Seasat scatterometer versus scanning multichannel microwave radiometer wind speeds: A comparison on a global scale*. J. Geophys. Res. 95 (12), 22275–22288. https://doi.org/10.1029/JC095iC12p22275

Balmaseda, M.A., Vidard, A., Anderson, D.L.T., 2008. *The ECMWF ocean analysis system: ORA-S3*. Mon. Weather Rev. 136 (8), 3018–3033. https://doi.org/10.1175/2008MWR2433.1

Bi, F., Song, J.B., Wu, K.J., Xu, Y., 2015. *Evaluation of the simulation capability of the Wavewatch III model for the Pacific Ocean wave*. Acta Oceanol. Sin. 34 (9), 43–57. https://doi.org/10.1007/s13131-015-0737-1

Booij, N., Ris, R.C., Holthuijsen, L.H., 1999. *A third-generation wave model for coastal regions: 1. Model description and validation*. J. Geophys. Res.-Oceans 104 (C4), 7649–7666. https://doi.org/10.1029/98JC02622

Chen, C.S., Liu, H., Beardsley, R.C., 2003. *An unstructured, finite-volume, three-dimensional, primitive equation ocean model: Application to coastal ocean and estuaries*. J. Atmos. Ocean. Technol. 20 (1), 159–186. https://doi.org/10.1175/1520-0426(2003)020<0159:AUGFVT>2.0.CO;2

Chen, Y., Chen, L., Zhang, H., Gong, W.P., 2019. *Effects of wave-current interaction on the Pearl River Estuary*

during Typhoon Hato. Estuar. Coast. Shelf S. 228 (11), 106364.
https://doi.org/10.1016/j.ecss.2019.106364

Chen, J.L., Hao, M.Y., Shao, W.Z., Marino, A., Hu, Y.Y., Song, X.G., 2024. *Validation of wind speed retrieval from HY-2B calibration microwave radiometer data during tropical cyclones*. Remote Sens. Lett. 15 (7), 700–708.
https://doi.org/10.1080/2150704X.2024.2368926

Elfouhaily, T., Chapron, B., Katsaros, K., 1997. *A unified directional spectrum for long and short wind-driven waves*. J. Geophys. Res.-Atmospheres, 102 (C7), 15781–15769.
https://doi.org/10.1029/97JC00467

Foli, B.A.K., Appeaning Addo, K., Ansong, J.K., Wiafe, G., 2022. *Evaluation of ECMWF and NCEP reanalysis wind fields for long-term historical analysis and ocean wave modelling in West Africa*. Remote Sens. Earth Syst. Sci. 5 (6), 26–45.
https://doi.org/10.1007/s41976-021-00052-3

Guan, S.D., and Coauthors, 2024. *Ocean internal tides suppress tropical cyclones in the South China Sea*. Nat. Commun. 15 (5), 3903.
https://doi.org/10.1038/s41467-024-48003-y

Hao, M.Y., Shao, W.Z., Shi, S., Liu, X., Hu, Y.Y., Zuo, J.C., 2023. *Validation of Surface Waves Investigation and Monitoring data against simulation by Simulating Waves Nearshore and wave retrieval from Gaofen-3 synthetic aperture radar image*. Remote Sens. 15 (18), 4402.
https://doi.org/10.3390/rs15184402

Hauser, D., Tison, C., Amiot, T., Delaye, L., Corcoral, N., Castillan, P., 2017. *SWIM: The first spaceborne wave scatterometer*. IEEE Trans. Geosci. Remote Sens. 55 (5), 3000–3014.
https://doi.org/10.1109/TGRS.2017.2658672

Hersbach, H., 2010. *Comparison of C-Band scatterometer CMOD5 equivalent neutral winds with ECMWF*. J. Atmos. Ocean. Technol. 27 (4), 721–736.
https://doi.org/10.1175/2009JTECHO698.1

Holthuijsen, L., 2001. *The continued development of the third-generation shallow water wave model 'SWAN'*. Tu Delft Dep. Hydraul. Eng. 32, 185–186.

Hu, Y.Y., Shao, W.Z., Wei, Y.L., Zuo, J.C. 2021. *Analysis of typhoon-induced waves along typhoon tracks in the western north Pacific Ocean, 1998–2017*. J. Mar. Sci. Eng. 8 (7), 521.
https://doi.org/10.3390/jmse8070521

Hu, Y.Y., Shao, W.Z., Xu, Y., Zou, Q.P., Jiang, X.W., 2024. *Improvement of drag coefficient parameterization of WAVEWATCH-III using remotely sensed products during tropical cyclones*. Ocean Dynam. 74 (9), 843–858.
https://doi.org/10.1007/s10236-024-01638-3

Huang, J.C., Ma, Z.H., Zhao, H.K., Fei, J.F., Chen, L.H. 2024. *Increase in Western North Pacific tropical cyclone intensification rates and their northwestward shifts*. Atmos. Res. 301 (5), 107292.
https://doi.org/10.1016/j.atmosres.2024.107292

Kalourazi, M.Y., Siadatmousavi, S.M., Yeganeh-Bakhtiary, A., Jose, F., 2020. *Simulating tropical storms in the Gulf of Mexico using analytical models*. Oceanologia 62 (2), 173–189.
https://doi.org/10.1016/j.oceano.2019.11.001

Lai, Z.Z., Hao, M.Y., Shao, W.Z., Shen, W., Hu, Y.Y., Jiang, X.W., 2023. *Wind field reconstruction based on dual-polarized synthetic aperture radar during a tropical cyclone*. Eur. J. Remote Sens. 56, 2273867.
https://doi.org/10.1080/22797254.2023.2273867

Li, X.H., Yang, J.S., Han, G.Q., Ren, L., Zheng, G., Chen, P., Zhang, H., 2022. *Tropical cyclone wind field reconstruction and validation using measurements from SFMR and SMAP radiometer*. Remote Sens. 14 (16), 3929.
https://doi.org/10.3390/rs14163929

Lin, I.I., Pun, I.F., Wu, C.C., 2009. *Upper-Ocean thermal structure and the Western North Pacific category 5 typhoons. Part II: dependence on translation speed*. Mon. Weather Rev. 137 (11), 3744–3757.
https://doi.org/10.1175/2009MWR2713.1

Liu, Y.H., Guan, H.D., Lin, I.I., Zhao, W., Jin, F.F., Liu, P., J. Tian, J.W., 2025. *Storm size modulates tropical cyclone intensification through an oceanic pathway in global oceans*. J. Climate 38 (4), 891–908.
https://doi.org/10.1175/JCLI-D-24-0398.1

Mei, W., Pasquero, C., 2013. *Spatial and temporal characterization of sea surface temperature response to tropical cyclones*. J. Climate 26 (11), 3745-3765.
https://doi.org/10.1175/JCLI-D-12-00125.1

Meissner, T., Ricciardulli, L., Wentz, F., 2017. *The capability of the SMAP mission to measure ocean surface winds in storms*. B. Am. Meteorol. Soc. 98 (8), 1660–1677.
https://doi.org/10.1175/BAMS-D-16-0052.1

Mellor, G.L., Yamada, T., 1982. *Development of a turbulence closure model for geophysical fluid problems*. Rev. Geophys. 20 (4), 851–875.
https://doi.org/10.1029/RG020i004p00851

Morozov, E.G., Velarde, M.G., 2008. *Inertial oscillations as a deep ocean response to hurricanes*. J. Oceangr. 64 (8), 495–509.
https://doi.org/10.1007/s10872-008-0042-0

Mouche, A.A., Chapron, B., Zhang, B., Husson, R., 2017. *Combined co and cross-polarized SAR measurements under extreme wind conditions*. IEEE Trans. Geosci. Remote Sens. 55 (12), 6476–6755.
https://doi.org/10.1109/TGRS.2017.2732508

Nittis, K., Perivoliotis, L., Korres, G., Tziavos, C., Thanos, I., 2006. *Operational monitoring and forecasting for marine environmental applications in the Aegean Sea*. Environ. Modell. Softw. 21 (2), 243–257.
https://doi.org/10.1016/j.envsoft.2004.04.023

Rogers, W.E., Hwang, P., Wang, W.D., 2003. *Investigation of wave growth and decay in the SWAN model: Three regional-scale applications*. J. Phys. Oceanogr. 33 (2),

366–389.
https://doi.org/10.1175/1520-0485(2003)033<0366:IOWGAD>2.0.CO;2

Shao, W.Z., Chen, J.L, Hu, S., Yang, Y.Q., Jiang, X.W., Shen, W., Li, H., 2024b. *Influence of sea surface waves on numerical modeling of an oil spill: Revisit of Symphony Wheel accident*. J Sea Res. 201 (10), 102529.
https://doi.org/10.1016/j.seares.2024.102529

Shao, W.Z., Hu, Y.Y., Lai, Z.Z., Zhang, Y.G., Jiang, W.W., 2023. *Rain rate retrieval algorithm for dual-polarized Sentinel-1 SAR in tropical cyclones*. IEEE Remote Sens. Lett. 20, 4011405.
https://doi.org/10.1109/LGRS.2023.3320351

Shao, W.Z., Hu, Y.Y., Migliaccio, M., Marino, A., Jiang, X.W., 2024a. *Machine learning-based algorithm for SAR wave parameters retrieval during a tropical cyclone*. IEEE J. Sel. Topics Appl. Earth Observ. Remote Sens. 17, 15166–15177.
https://doi.org/10.1109/JSTARS.2024.3445129

Shao, W.Z., Jiang, T., Jiang, X.W., Zhang, Y.G., Zhou, W., 2021. *Evaluation of sea surface winds and waves retrieved from the Chinese HY-2B data*. IEEE J. Sel. Topics Appl. Earth Observ. Remote Sens. 14, 9624–9635.
https://doi.org/10.1109/JSTARS.2021.3112760

Shao, W.Z., Jiang, X.W., Sun, Z.F., Hu, Y.Y., Marino, A., Zhang, Y.G., 2022. *Evaluation of wave retrieval for Chinese Gaofen-3 synthetic aperture radar*. Geo-spat. Inf. Sci. 25 (2), 229–243.
https://doi.org/10.1080/10095020.2021.2012531

Shen, H., Perrie, W., He, Y.J., Liu, G., 2014. *Wind speed retrieval from VH dual-polarization RADARSAT-2 SAR images*. IEEE Trans. Geosci. Remote Sens. 52 (9), 5820–5826.
https://doi.org/10.1109/TGRS.2013.2293143

Shi, J., Shao, W.Z., Shi, S.H., Hu, Y.Y., Jiang, T., Zhang, Y.G., 2023. *Can sea surface waves be simulated by numerical wave models using the fusion data from remote-sensed winds?* Remote Sens. 15 (15), 3825.
https://doi.org/10.3390/rs15153825

Steele, K., Lau, J., Hsu, Y.H., 1985. *Theory and application of calibration techniques for an NDBC directional wave measurement buoy*. IEEE J. Oceanic Eng. 10 (4), 382–396.
https://doi.org/10.1109/JOE.1985.1145116

Stepanov, V.N., Haines, K., 2014. *Mechanisms of Atlantic meridional overturning circulation variability simulated by the NEMO model*. Ocean Sci. 10 (4), 645–656.
https://doi.org/10.5194/os-10-645-2014

Stopa, J.E., Cheung, K.F., 2014. *Intercomparison of wind and wave data from the ECMWF reanalysis interim and the NCEP climate forecast system reanalysis*.
Ocean Model. 75 (3), 65–83. https://doi.org/10.1016/j.ocemod.2013.12.006

Tolman, L., 1991. *A third-generation model for wind waves on slowly varying, unsteady, and inhomogeneous depths and currents*. J. Phys. Oceanogr. 21 (6), 782–797.
https://doi.org/10.1175/1520-0485(1991)021<0782:ATGMFW>2.0.CO;2

Vickers, D., Mahrt, L., Andreas, E.L., 2013. *Estimates of the 10-m neutral sea surface drag coefficient from aircraft eddy covariance measurements*. J. Phys. Oceanogr. 43 (2), 301–310.
https://doi.org/10.1175/JPO-D-12-0101.1

Vogelzang, J., Stoffelen, A., 2017. *ASCAT ultrahigh-resolution wind products on optimized grids*. IEEE J. Sel. Topics Appl. Earth Observ. Remote Sens. 10 (5), 2332–2339.
https://doi.org/10.1109/JSTARS.2016.2623861

Wang, Q.H., Shi, J., Xia, J.M., Han, K.F., Xiao, W.B., Zhang, W.J., Wang, H.D., Lv, J.L., 2023. *Influence of wave-induced radiation stress on upper-layer ocean temperature during typhoons*. Remote Sens. 15 (9), 2442. https://doi.org/10.3390/rs15092442

Wei, H., Hainbucher, D., Pohlmann, T., Feng, S., Suendermann, J., 2004. *Tidal-induced Lagrangian and Eulerian mean circulation in the Bohai Sea*. J. Marine Syst. 44 (3–4), 141–151.
https://doi.org/10.1016/j.jmarsys.2003.09.007

Wei, M., Shao, W.Z., Shen, W., Hu, Y.Y., Zhang, Y., Zuo, J.C., 2024. *Contribution of surface waves to sea surface temperatures in the Arctic Ocean*. J. Ocean Univ. China 23 (10), 1151–1162.
https://doi.org/10.1007/s11802-024-5797-4

Weisberg, R.H., Zheng, L., 2008. *Hurricane storm surge simulations comparing three-dimensional with two-dimensional formulations based on an Ivan-like storm over the Tampa Bay, Florida Region*. J. Geophys. Res.-Oceans 113 (12), C12001.
https://doi.org/10.1029/2008JC005115

Wentz, F.J., 1992. *Measurement of oceanic wind vector using satellite microwave radiometers*. IEEE Trans. Geosci. Remote Sens. 30 (5), 960–972.
https://doi.org/10.1109/36.175331

Wu, J., 1982. *Wind-stress coefficients over the sea surface from breeze to hurricane*. J. Geophys. Res-Oceans 87 (C12), 9704–9706.
https://doi.org/10.1029/JC087iC12p09704

Wu, R.H., Zhang, H., Chen, D.K., 2020. *Effect of Typhoon Kalmaegi (2014) on the northern South China Sea explored using multi-platform satellite and buoy observations data*. Prog. Oceanogr. 180 (1), 102218.
https://doi.org/10.1016/j.pocean.2019.102218

Yang, B., Hou, Y.J., Li, M., 2019. *Response of the western North Pacific subtropical ocean to the slow-moving Super Typhoon Nanmadol*. J. Oceanol. Limnol. 37 (5), 938–956.
https://doi.org/10.1007/s00343-019-8114-0

Yao, F.C., Johns, W.E., 2010. *A HYCOM modeling study of the Persian Gulf: 1. Model configurations and surface circulation*. J. Geophys. Res.-Oceans. 115 (C11), C11017.
https://doi.org/10.1029/2009JC005781

Yao, R., Shao, W.Z., Hao, M.Y., Zuo, J.C. Hu, S., 2023. *The response of waves to the sea surface temperature in the context of global change*. Remote Sens. 15 (7), 1948.

Zhang, Z.X., Qi, Y.Q., Shi, P., Li, C.W., Li, Y., 2003. *Preliminary study on assimilation of significant wave heights from T/P altimeter*. Acta Oceanol. Sin. 25 (5), 21–28. http://hdl.handle.net/10397/68190

Zheng, P., Li, M., van der A, D.A., van der Zanden, J., Wolf, J., Chen, X., Wang, C.X., 2017. *A 3d unstructured grid nearshore hydrodynamic model based on the vortex force formalism*. Ocean Model. 116 (8), 48–49. https://doi.org/10.1016/j.ocemod.2017.06.003

Zhou, Y.S., Li, J., Zhang, H., Chen, Z., Zhang, L., Wang, P., 2022. *Internal calibration for airborne X-band DBF-SAR imaging*. IEEE Remote Sens. Lett. 19, 4008105. https://doi.org/10.1109/LGRS.2020.3047874

Zhou, Y.H., Shao, W.Z., Nunziata, F., Wang, W.L., Li, C., 2024. *An algorithm to retrieve the range ocean current speed under tropical cyclone conditions from Sentinel-1 synthetic aperture radar measurements based on XGBoost*. Remote Sens. 16 (17), 3271. https://doi.org/10.3390/rs16173271